Volume 5
Number 7
7 April 2024
Pages 2609–3068

Materials Advances

rsc.li/materials-advances

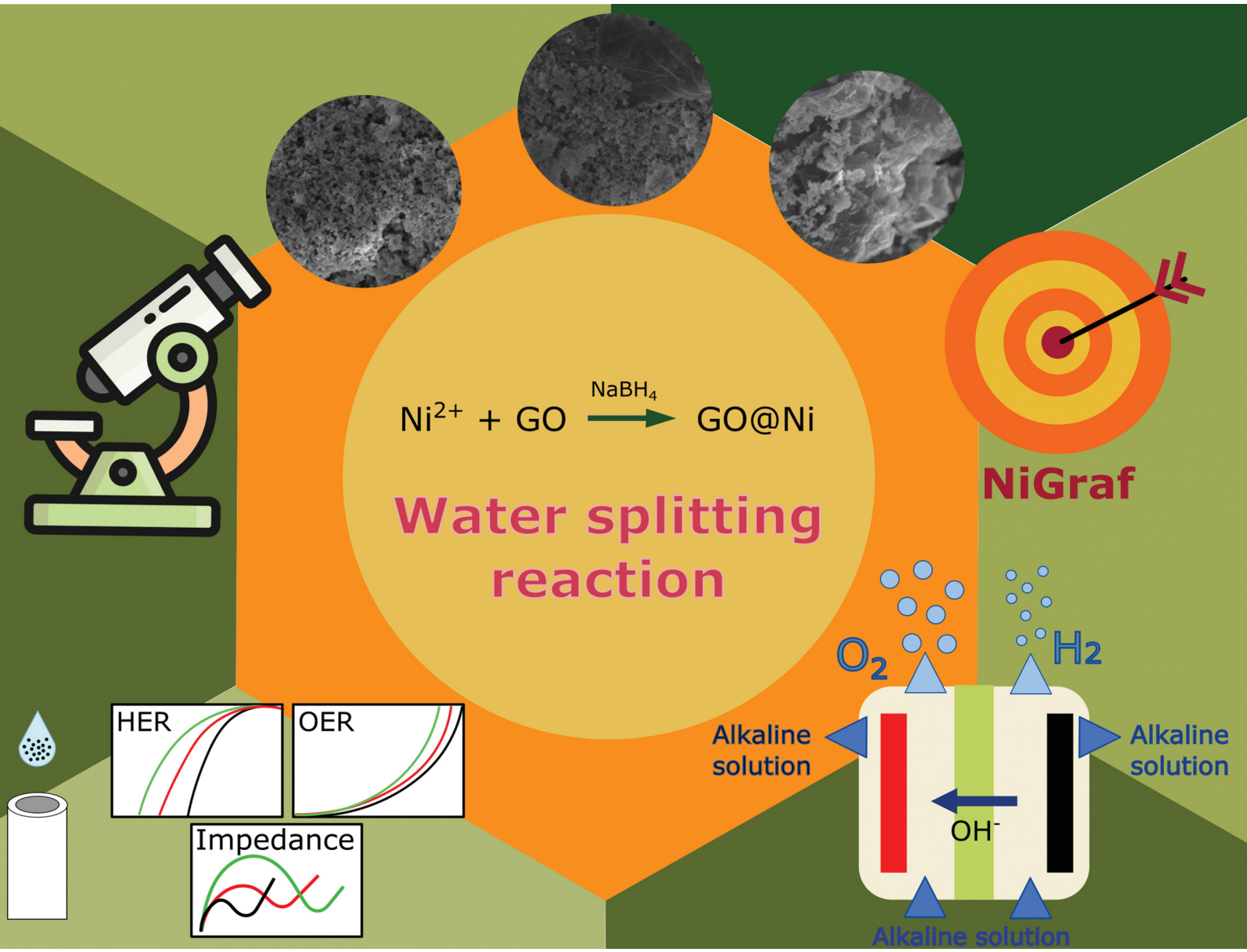

ISSN 2633-5409

ROYAL SOCIETY OF CHEMISTRY

PAPER
Mario Pagliaro, Cinzia Giannini, Rosaria Ciriminna, Alessandro Lavacchi *et al.*
NiGraf: a new nickel-based molecularly doped metal for enhanced water electrolysis

Materials Advances

ROYAL SOCIETY OF CHEMISTRY

PAPER

View Article Online
View Journal | View Issue

Cite this: *Mater. Adv.*, 2024, 5, 2759

NiGraf: a new nickel-based molecularly doped metal for enhanced water electrolysis†

Mario Pagliaro, *[a] Maria V. Pagliaro, [b] Rocco Caliandro, [c] Cinzia Giannini, *[c] Rosaria Ciriminna *[a] and Alessandro Lavacchi *[b]

Received 12th September 2023,
Accepted 19th December 2023

DOI: 10.1039/d3ma00700f

rsc.li/materials-advances

Graphene oxide was 3D entrapped in nickel-based nanoparticles *via* the molecularly doped metal approach and the resulting nanostructured material applied as electrocatalyst in both hydrogen and oxygen evolution reactions at room temperature. This establishes a completely new class of catalytic materials, dubbed herein "NiGraf", which is highly promising towards enhanced alkaline water electrolysis.

The production of hydrogen *via* water electrolysis, using low cost electricity from renewable energy sources (sun, water and wind), is a key technology to store intermittent renewable energy in the chemical energy of the hydrogen molecule.[1] Currently, alkaline water electrolysis (AWE) at the surface of low cost nickel-based electrodes in electrolysis cells operated at 80 °C in 30% KOH,[2] is used worldwide to produce about 1% of the global amount of hydrogen (55 million t) manufactured yearly.[3] Lowering the production cost of electrolytic H_2 made *via* AWE (today amounting to 5.50 € per kg)[4] requires the development of more efficient electrodes, by lowering the electrolytic cell overpotential while retaining the high electrocatalyst durability typical of Ni-based electrocatalysts.

Commercial maturity has also been reached by Proton Exchange Membrane Water Electrolysis (PEMWE) that allows sustained operations at more than 2 A cm^{-2} but with the significant drawback of using large amount of expensive and rare platinum group metals (PGM), particularly Pt and Ir.

In the last decade a novel technology that combines the high productivity PEMWEs with the use of non critical resources of AWE has emerged, namely a new class of electrolyzers known as Alkaline Membrane Water Electrolyzers (AMWEs) that employ anion exchange membranes as separators and can operate with PGM-free catalysts,[5] making the technology efficient and inexpensive.[6] In AMWEs, nickel-based electrocatalysts are widely used both at the cathode to mediate the hydrogen evolution reaction (HER) and at the anode to catalyze the oxygen evolution reaction (OER).[7] Adding to their technical and economic viability, Ni-based catalysts can be fabricated *via* easy to scale-up and high-throughput processes.[8] Recent insights suggest that new nanostructured or single-atom catalysts, coupled to 3D printing for the fabrication of large area electrodes,[9] are among the most promising routes to achieve the ambitious goal of developing a critical raw material free strategy to produce green hydrogen.[10]

Dubbed "NiGraf", in this work we introduce of a new class of Ni-based nanostructured catalysts consisting of Ni-based nanoparticles eencapsulating the graphene moiety. Also known as metal–organic alloys (MORALs),[11] molecularly doped metals (organics@metal) have shown great potential in improving H_2 and O_2 recombination in fuel cells. For instance, Dekel and Avnir have lately demonstrated the applications of ionomer@Ag MORALs to boost the performance of anion-exchange membranes in fuel cells.[12]

Graphene has been widely investigated as dopant of different nickel/graphene electrocatalysts for water electrolysis. For instance, nickel nanoparticles functionalized with graphene *via* electrophoretic deposition were adopted as catalyst of enhanced HER performance in alkaline solution with overpotential of 65 mV for 10 mA cm^{-2} retaining the prolonged stability of Ni-based electrocatalysts.[13] Similarly, Ni sponge functionalized with nitrogen-doped graphene,[14] as well as graphene layer/nickel foam obtained by chemical vapor deposition (in presence of methane at high temperature),[15] showed very high HER activity. Now, we describe the encapsulation of graphene moiety in nickel-based nanoparticles (NPs).

The straightforward and highly reproducible catalyst synthesis, lately described for the encapsulation of GO in Pd nanoparticles,[16] involves concomitant dissolution in water of

[a] *Istituto per lo Studio dei Materiali Nanostrutturati, CNR, via U. La Malfa 153, Palermo 90146, Italy. E-mail: mario.pagliaro@cnr.it, rosaria.ciriminna@cnr.it*
[b] *Istituto di Chimica dei Composti Organometallici, CNR, via Madonna del Piano 10, Sesto Fiorentino FI 50019, Italy. E-mail: alessandro.lavacchi@cnr.it, mpagliaro@iccom.cnr.it*
[c] *Istituto di Cristallografia, CNR, via G. Amendola 1220, Bari 70126, Italy. E-mail: cinzia.giannini@cnr.it, rocco.caliandro@cnr.it*

† Electronic supplementary information (ESI) available. See DOI: https://doi.org/10.1039/d3ma00700f

Table 1 NiGraf sample name and GO load

Name	GO load (wt%)
NG1	0.2
NG2	1.0
NG3	5.0

graphene oxide (GO) and a nickel salt followed by reduction of the metal cations with a reducing agent (eqn (1)),

$$Ni^{2+} + GO \xrightarrow{NaBH_4} GO@Ni \quad (1)$$

Three NiGraf materials at different GO load (Table 1) were isolated as highly hydrophilic powders colored in deep black.

We briefly remind that MORALs substantially differ from composite materials. The latter are surface-heterogenized materials in which a substance is physically or chemically 2D adsorbed at the surface, in general for a relatively short depth of the hosting material (2D adsorption normally uses only one moiety of the adsorbed molecules, and usually affecting only the metallic atoms at the interface, not the bulk). MORALs, on the other hand, are molecularly doped metals in which the dopant species is 3D entrapped within the metal crystal lattice.[11]

The high resolution TEM (HR-TEM) photographs in Fig. 1 show the morphology of different zones of the as-prepared NG1, NG2 and NG3 samples at low (left column) and high (right column) magnifications. The photographs reveal the presence of Ni-based globular structures and glassy GO sheets on the edge of the aggregated nanoparticles, as well as of Ni-based aggregated nanoparticles intertwined with GO regions.

Fig. 2 displays the scanning transmission electron microscope (STEM) images in brightfield (A), darkfield (B) and high-angle annular dark-field (C) mode, alongside with the related Carbon (D), Nickel (E), Oxygen (F) elemental maps for sample NG3, the NiGraf containing the highest load of graphene oxide. Fig. 2E and F show that Ni is largely present in oxidised form. The spatial distribution of oxygen, indeed, follows that of nickel.

The low magnification SEM analysis (Fig. S7 in the ESI†) shows a different morphology for each sample: the presence of a growing quantity of graphene leads to a more compact structure composed of smaller Ni-based particles. In NG1 sample, the GO coverage is less uniform, as evident at higher magnification (Fig. S7B and C, ESI†), while in NG3 the high amount of graphene oxide results in the packing of GO sheets in certain areas. Said otherwise, the fact that upon increasing the GO concentration, one can clearly observe GO platelets surrounding the NiGraf particles confirms that a threshold exists beyond which the large (polymeric) GO planar molecules are no longer 3D entrapped within the Ni and jamborite (see below) native particles formed during the reductive entrapment process taking place in solution, followed by precipitation of the 3D functionalized metal nanoparticles. Beyond that threshold, the GO platelets end up surrounding the outer surface of the as-formed NiGraf nanoparticles. The XRD diffractograms of the NiGraf materials (Fig. 3) indicate a reduced crystallinity (broader peaks) for the samples with the highest GO loads (NG2 and NG3).

The main crystal phase present in the XRD profile of NG1 was identified as the jamborite crystal structure (COD #9012316) (Fig. S1, ESI†). It can be easily distinguished from the β-$Ni(OH)_2$ polymorph (theophrastite) which should reveal the presence of the basal peak at $2\theta = 11^\circ$ (Fig. S2, ESI†). The corresponding Rietveld fit, for the jamborite structure, is shown in Fig. 4.

These findings already suggest that the NiGraf materials consist of graphene oxide entrapped in jamborite ($Ni(OH)_2$(NiOOH), *syn*) nanoparticles. To substantiate this statement, we have performed a structural analysis of the NiGraf samples carried out on Pair Distribution Function (PDF) profiles, which for nanomaterials may be more informative than XRD profiles. The superposition of the measured profiles (Fig. 5) indicates that the local order is limited to about 9 Å for samples with higher GO load (NG2 and NG3). Moreover, the position of the peaks distinguishable in three samples is retained in all different materials, showing evidence that the same crystal phase composition is present in each material, independent of the GO load.

Even more importantly, the PDF reveals the presence of a clear first peak at interatomic distance $r = 1.48$ Å, which cannot be attributed to a ($Ni(OH)_2$(NiOOH), *syn*) jamborite crystal phase (the Ni–O bond length is 1.97 Å, which coincides with the second peak of the PDF profiles). As shown in the following (Fig. 6) this peak can be fitted by considering a GO crystal phase, thereby proving that graphene oxide is present in all NiGraf samples.

Identification of the correct GO crystal phase was achieved by applying Principal Component Analysis (PCA) on observed and calculated PDF profiles (Fig. S3, ESI†). This analysis ruled out the presence of extended sheets of graphene, in favor of carbon clusters of limited size (Table S1, ESI†). The GO crystal phase best describing data (COD #9012236) was singled out among those selected by PCA by performing repeated fits of the experimental PDF profiles of the three NiGraf samples by using a combination of jamborite and GO crystal phases. The best fits are shown in Fig. 6. The structural parameters determined by the PDF fit are reported in Table S2 (ESI†). The values of the scale parameter, which determine the weight fraction of the jamborite phase in the two-phases model fitting the NiGraf samples, correlate with the score values obtained *via* PCA applied on PDF profiles (Fig. 7).

This result indicates that the order–disorder transition occurring when increasing the GO load is the result of a reduction of the amount of crystalline ($Ni(OH)_2$(NiOOH)) jamborite, in fair agreement with what is deduced by visual inspection of Fig. 5. In addition, the fitted values of the particle diameter for the PDF shape damping function ($SP_{diameter}$ parameter in Table S2, ESI†) suggest that the increase in GO load is accompanied by changes of the average size of the crystalline domains, in agreement with the values estimated by Scherrer single peak analysis on common peaks among XRD profiles (Fig. S4, ESI†). We have also verified (data not shown) that a fit based on a core–shell model of GO wrapped Ni nanoparticles does not lead to better results.

Formation of jamborite, rather than metallic Ni in the presence of GO during reduction of Ni^{2+} with an excess of sodium

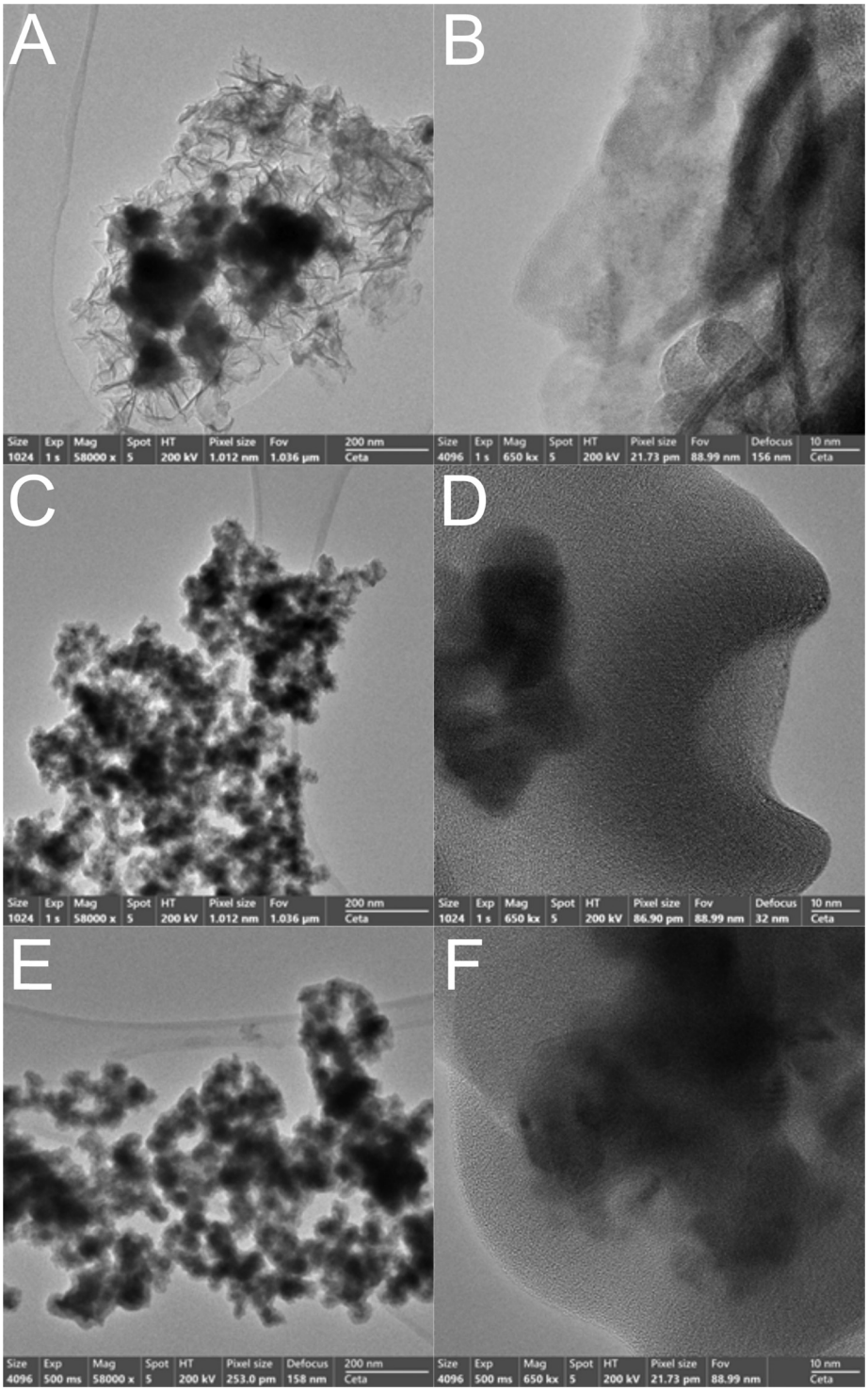

Fig. 1 HR-TEM images at low (left column) and high (right column) magnification (58 Kx and 650 Kx) of NiGraf NG1-2-3 samples with increasing load of graphene oxide: (A) and (B) 0.2% GO, (C) and (D) 1% GO, (E) and (F) 5% GO. Scale bar of 200 nm for the low magnification (left column) and 10 nm for the high magnification (right column).

borohydride, suggests that GO acts as oxidation catalyst, a well-known feature of GO chemistry.[17] Likely, in the presence of air's oxygen GO promotes oxidation of the as-formed Ni^0 nanoparticles. In water only, indeed, the borohydride anion is an excellent reducting agent promoting the quick and complete conversion of Ni^{2+} into Ni nanoparticles already a $[Ni^{2+}]:[BH_4^-]$ 1:1 ratio rather than at the 2:1 ratio of eqn (2):[18]

$$2Ni^{2+} + BH_4^- + 4H_2O \rightarrow B(OH)_4^- + 2Ni^0 + 4H^+ + 2H_2 \quad (2)$$

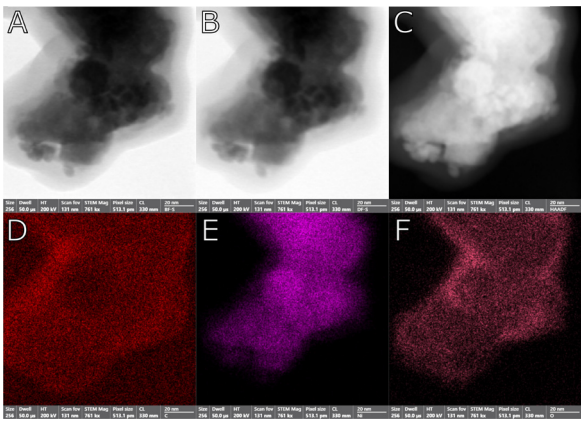

Fig. 2 STEM images of NG3 (5% GO) sample (A) brightfield, (B) darkfield, (C) high-angle annular dark-field imaging, and related element map (D) carbon (E) nickel (F) oxygen. Magnification: 760 000×, scale bar: 20 nm.

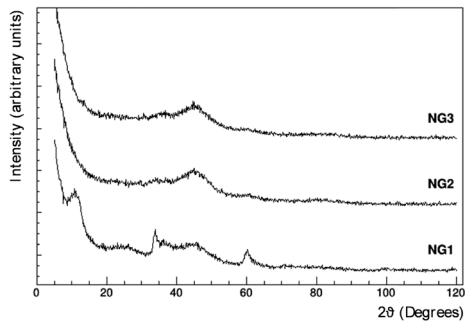

Fig. 3 XRD diffractograms for NG1, NG2 and NG3 NiGraf materials.

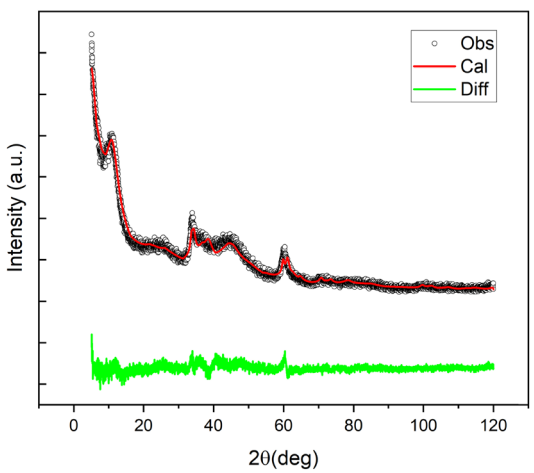

Fig. 4 Observed (black), Rietveld fitted (red), and difference (green) profiles of the XRD profile of NiGraf sample NG1.

The three Ni-based hybrid NiGraf materials at different load of GO were therefore tested through half-cell experiments for HER and oxygen evolution reaction (OER) in alkaline media. In order to quantitatively compare the HER and OER performance of all catalysts, we measured the polarization curves in H_2- or O_2-saturated KOH 0.1 M at room temperature with a scan rate of 1 mV s^{-1} and a rotation speed of 1600 rpm.

Interestingly the catalysts showed a different trend for the two reactions. As shown in Fig. 8A, the NiGraf material with the lowest GO load (NG1, 0.2% GO) exhibits the highest activity (2.2 mA mg_{cat}^{-1}) and the lowest onset potential, whereas the sample with the highest GO content (NG3, 5% GO) had the poorest HER performance. In other words, the HER trend indicates that the catalytic activity decreases with increasing the GO content. The entrapment of GO in the crystal lattice of Ni and nickel hydroxide nanoparticles may be responsible for this behavior. Interestingly, this behaviour is the opposite of Ni and ($Ni(OH)_2$(NiOOH)) jamborite nanoparticles encapsulated in graphite layers which exert a protective function.[19] A phenomenon that was ascribed to the increased tendency to reduce NiO_x (to Ni^0), a crucial stage for enhancing the efficacy and stability of Ni-based HER electrocatalysts.[19]

On the other hand, Fig. 8B shows evidence that the entrapment of increasing amounts of GO in the lattice of the jamborite nanoparticles facilitates Ni oxidation, as shown by the lowering of the peak onset associated with the Ni^{2+} – $N^{3+\delta}$ transition (from 1.39 V in NG1 to 1.35 V in NG3). Said nickel oxidation step is essential to activate the electrocatalyst for the OER. Accordingly, an increase in the amount of GO sheets entrapped in the jamborite crystal lattice results in improved OER activity. Said beneficial effect might be due to the overlap between the electrons in the valence shell of GO and those in the valence shell of Ni^{2+} which facilitates electron flow from the Ni^{2+} catalytic centers, eventually enabling formation of active $Ni^{3+\delta}$ at a reduced potential, and thus promoting the catalytic process.[20]

Finally, the potential required for water oxidation to obtain the current density of 20 mA mg_{cat}^{-1} was used to evaluate the OER specific activity. The samples with the highest amounts of GO (NG3 with 5% of GO and NG2 with 1% GO) present the smallest overpotential for OER, respectively 410 mV (1.64 V *vs.* RHE) and 450 mV (1.68 V *vs.* RHE), significantly lower than in the case of NG1 (0.2% GO) which has modest OER activity (it would have an overpotential greater than 600 mV). Table 2 summarizes the extrapolated electrochemical data.

The electrochemical impedance spectroscopy (EIS) results (see Fig. S6 and Table S3 in ESI†) show that OER is a more favorable reaction on the surface of NiGraf catalysts than HER and highlight a different trend for catalysts. The three NG NiGraf samples exhibited in general lower charge transfer resistance for OER, with growing R_{CT} values in the order NG3 > NG2 > NG1 as expected, confirming that NG3 is the most active catalyst. Moreover, NG2 and NG3 samples exhibit similar C_{dl} values, one order of magnitude larger with respect to NG1. EIS results for HER demonstrate that this reaction is more sluggish with respect to OER, with substantially higher R_{CT} values, especially for the NG3 sample with the highest GO content. This finding is particularly promising, in light of forthcoming practical applications, because the OER process is usually the most sluggish half-reaction in alkaline water electrolysis due to the multi-electron transfer process.[22]

In conclusion, the new findings reported in this study provide the proof of concept that the 3D entrapment of

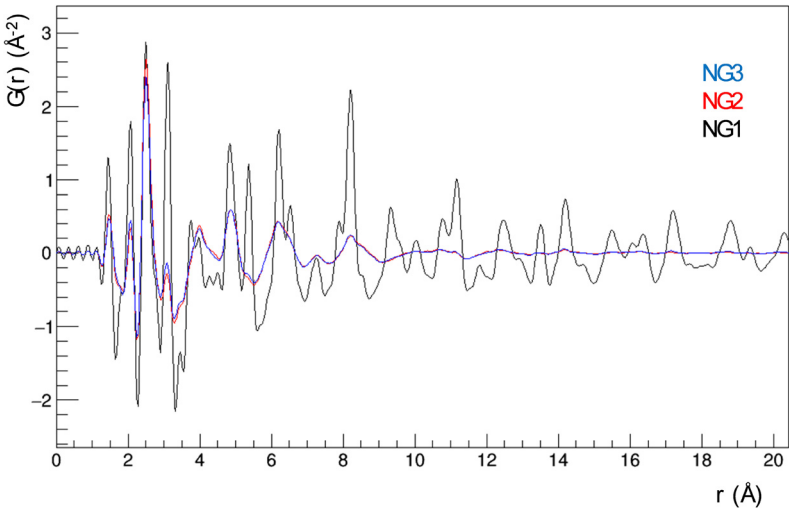

Fig. 5 PDF profiles for NG1, NG2 and NG3 NiGraf materials.

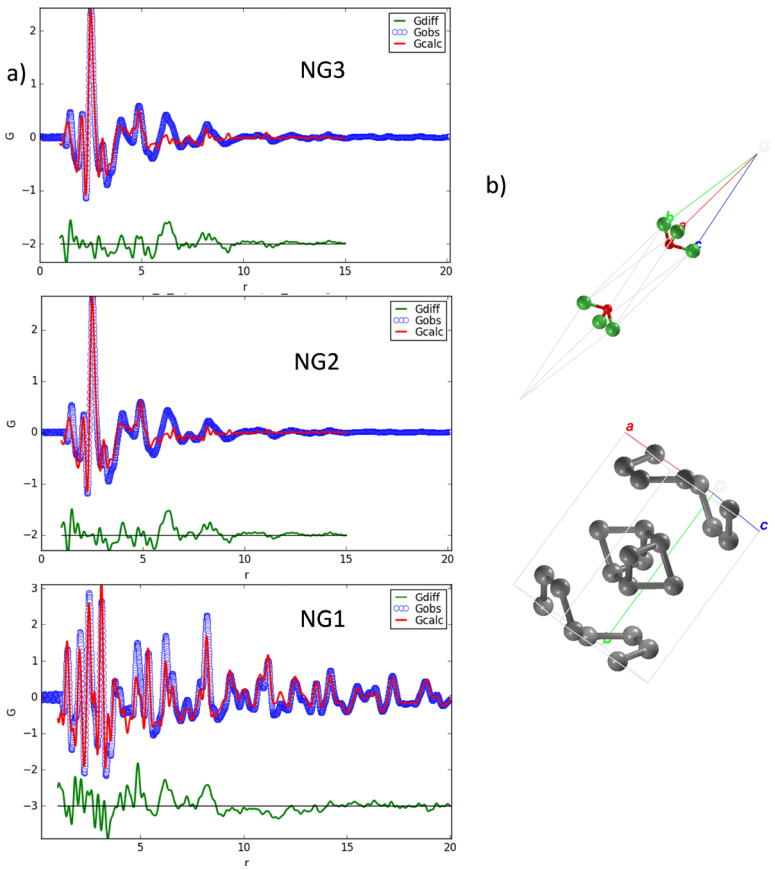

Fig. 6 Fit of the PDF profiles of the three NiGraf samples (experimental data = blue circles, fit curves = red line, residuals = green line) (a) by using a structural model obtained by combining linearly the crystal phases jamborite, COD #9012316 and GO, COD #9012236 (b). Atoms color code: C = gray; O = red; Ni = green.

graphene oxide in the lattice structure of jamborite *via* the molecularly doped metal approach of eqn (1) is possible, and that the resulting "NiGraf" molecularly doped metal nanomaterial is suitable to be used as electrocatalyst for both the HER and OER conversions of relevance in alkaline water electrolysis.

These preliminary results are highly promising towards the development of advanced, new generation Ni-based nanostructured catalysts capable to further lower the cost of electrolytic hydrogen.[9] Highly stable and easily dispersable in aqueous systems, MORAL hybrid metal nanoparticles such as those

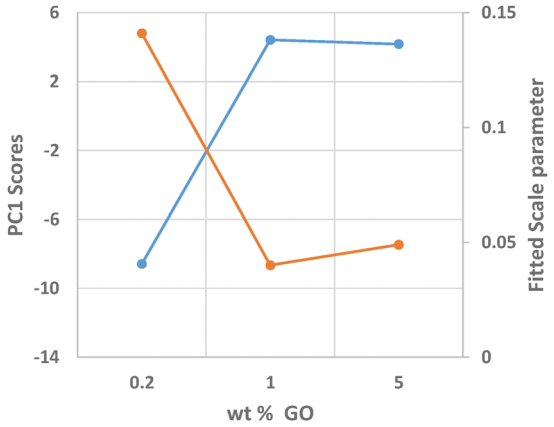

Fig. 7 Scores values of the first principal component, which explains 99.7% of the total data variance, determined *via* PCA applied on the PDF profiles (blue line, left vertical axis) and scale parameter of the jamborite crystal phase determined by fitting them (orange line, right vertical axis) as a function of the GO load (wt%) in the sample.

comprising the NiGraf material class, indeed, are especially well suited for use in continuous flow processes.[21] Future industrial production of electrolytic H_2 *via* AWE, in fact, will ideally take place under continuous flow conditions minimizing the electrolytic cell size and maximizing productivity.[23]

Experimental section

Three NiGraf materials were prepared by encapsulating graphene oxide with a theoretical load of GO between 0.2 and 5 wt% within Ni-based nanoparticles. The materials were prepared adding to a solution of $NiCl_2(H_2O)_6$ in 50 mL aqueous ethanol (H_2O: EtOH 1 : 1) purchased from Sigma Aldrich (Merck Life Science, Milan, Italy) kept under stirring different aliquots of an aqueous solution of graphene oxide (8 mg mL^{-1}, Nanografi Nano Teknoloji, Istanbul, Turkyie). After 30 min stirring, the mixture was added with an excess of an aqueous solution of $NaBH_4$ (99% purity, Sigma Aldrich). The reaction mixture immediately turned into a deeply black color. The reaction mixture was sealed and left under stirring for 24 h after which a black powder was isolated *via* simple filtration. Washed extensively with aqueous ethanol and thus with ultrapure water the material was left to dry at room temperature for 24 h. High-resolution HR-TEM and STEM was performed employing a Talos F200X G2 TEM microscope (Thermo Scientific). By exploiting its circular four-detector SuperX Energy Dispersive detector, high-resolution EDX maps of the Ni-based material samples were acquired. A drop of a sample solution (a small quantity of NiGraf material dispersed in an isopropanol) was dropcasted on a Holey TEM Copper grid used as a sample holder for the characterization. Scanning electron microscopy (SEM) experiments were performed by using a Tescan GAIA3 field emission SEM (Tescan Group, Brno, Czechia). To acquire the data presented in this study, the system operated at 5 kV.

The XRD patterns of NiGraf powders were collected by a Rigaku RINT2500 rotating anode diffractometer (50 kV, 200 mA) equipped with a silicon strip Rigaku D/teX Ultra detector. An asymmetric Johansson Ge(111) crystal is used to select the monochromatic Cu Kα1 radiation (λ = 1.54056 Å). Measurements were executed in transmission mode, by introducing the sample powder in a Lindemann capillary tube with a diameter of 0.5 mm, and scanning the 2θ angle continuously from 5° to 120° with a step size of 0.02°. The collected patterns were compared by principal component analysis (PCA) and Scherrer single peak analysis by using the RootProf program.[24] The profile of the most crystalline sample (NG1) was analyzed by the program QUALX[25] for crystal phase identification. The

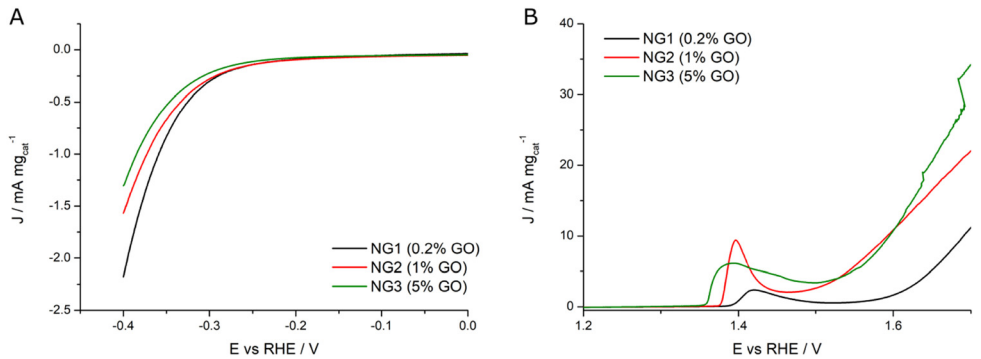

Fig. 8 (A) HER LSVs and (B) OER LSVs registered in KOH 0.1 M at 1 mV s^{-1} and 1600 rpm for NG1 (black curve), NG2 (red curve) and NG3 (green curve) samples.

Table 2 Extrapolated electrochemical performance data for different NiGraf electrocatalysts

Catalyst	E_{onset} (HER)/V	$\lvert J\rvert$/mA mg_{cat}^{-1} @0.4 V	E_{onset}/V Ni(II) → Ni(III + δ)	J/mA mg_{cat}^{-1} @ 1.7 V (OER)	η (OER)/V @ 20 mA mg_{cat}^{-1}
NG1 (0.2% GO)	0.276	2.2	1.389	11.1	>0.600
NG2 (1% GO)	0.278	1.6	1.375	22.0	0.450
NG3 (5% GO)	0.294	1.3	1.355	34.2	0.410

full-pattern fit of the identified phase (jamborite, AMCSD 0015759, COD 9012316) was performed on the measured pattern by means of the Rietveld method[26] implemented in the program EXPO2014.

The PDF profiles were obtained at the 28ID-2 beamline of the National Synchrotron Light Source (NSLS-II) of the Brookhaven National Laboratory with an X-ray energy of 68.36 keV (0.1814 Å) and a 0.5 mm × 0.5 mm beam size. A PerkinElmer XRD 1621 digital imaging detector having 2048 × 2048 pixels with size 200 × 200 μm, was mounted orthogonal to the beam path at 206 mm downstream of the sample. Cerium oxide was measured as a standard material to calibrate the wavelength and the detector position. An empty capillary was measured for background estimation. Diffraction images were azimuthally integrated and converted into intensity profiles *vs.* momentum transfer $Q = 4\pi \sin\theta/\lambda$ by using the DIOPTAS program.[27] PDF profiles were calculated from the Q profiles with the program PDFGetX3.[28] The parameters for PDF calculation (background subtraction, scale factor, minimum and maximum values of Q, degree of data-correction polynomial) were optimized on individual PDF profiles, to avoid large termination effects and preserve the signal to noise ratio. The Q_{max} values were 23.5 $Å^{-1}$ for the three NiGraf samples. The structural refinement of PDF profile was executed by using PDFGUI[29] and Diffpy-CMI[30] (core–shell analysis).

The electrochemical tests were performed in a standard three electrode system using a potentiostat (Parstat 2273) equipped with a Model 616 rotating disk electrode RDE (PAR-Ametek). A 5 mm (A = 0.1963 cm^2) Teflon-potted glassy-carbon disk electrode tip (PINE) was used as substrate for the deposition of the catalyst ink, while an Ag/AgCl (KCl sat.) and a gold wire were used, respectively, as reference and counter electrode. All potentials were calibrated to the reversible hydrogen electrode (RHE) scale. The catalyst ink was prepared by sonicating 7 mg of catalyst in a hydroalcoholic solution (50 : 50 H_2O : EtOH) and 12 mg of 5% Nafion ionomer solution. The experiments were undertaken in 0.1 M aqueous KOH (Sigma-Aldrich, 99.8%) prepared with Millipore water (18 MΩ cm^{-1}) provided with a VWR Puranity TU 3 system. Linear scan voltage (LSV) were acquired at 1 mV s^{-1} and 1600 rpm to probe HER (from 0 to −0.4 V *vs.* RHE) and OER activity of the catalysts (from 1.2 to 1.7 V *vs.* RHE). Tafel analysis was then performed through linear fitting of the $\log i$ *vs.* Potential curves (Tafel plot). EIS analysis were conducted at a fixed constant potential, −0.3 V *vs.* RHE to study HER, and at 1.6 V in the case of OER.

Data availability

All data are available upon reasonable request by contacting the corresponding authors.

Conflicts of interest

The authors declare no competing financial interest.

Acknowledgements

We thank the Ministry of Enterprises and Made in Italy for funding under the Piano Operativo della Ricerca "Ricerca e sviluppo sull'idrogeno" financed by the EU – NextGenerationEU – M2C2 Investment 3.5, "LA 1.1.6 – Sviluppo di materiali e componenti non contenenti materiali critici per elettrolizzatori anionici (AEM) operanti anche ad elevata pressione differenziale". We thank Dr Salvatore Romeo, Istituto per lo Studio dei Materiali Nanostrutturati, CNR, for administrative assistance and Rocco Lassando, Istituto di Cristallografia, CNR, for his support in carrying out the synchrotron experiment. The access to the National Synchrotron Light Source, Brookhaven National Laboratory, was supported by the U.S. Department of Energy, Office of Science, Office of Basic Energy Sciences, under Contract No. DE-SC0012704 (NSLS-II Proposal Number 312211).

References

1 M. Pagliaro and A. G. Konstandopoulos, *Solar Hydrogen*, RSC Publishing, Cambridge, 2012.
2 N. Guillet and P. Millet, Alkaline Water Electrolysis, in *Hydrogen Production*, ed. A. Godula-Jopek, Wiley-VCH, Weinheim, 2015, pp.117–166.
3 Hydrogen Council, Hydrogen scaling up, Brussels: 2017. **https://hydrogencouncil.com/wp-content/uploads/2017/11/Hydrogen-Scaling-up_Hydrogen-Council_2017.compressed.pdf** (accessed December 6, 2023).
4 H. Bergmann, Aus der Geschichte der Wasserelektrolyse - Wie es einst began. Mit einer Diskussion der Perspektiven, *Galvanotechnik*, 2017, **108**, Teil 1: 44–49; Teil 2: 260–267, Teil 3: 471–479.
5 (*a*) H. A. Miller, K. Bouzek, J. Hnat, S. Loos, C. I. Bernäcker, T. Weißgärber, L. Röntzsch and J. Meier-Haackd, Green hydrogen from anion exchange membrane water electrolysis: a review of recent developments in critical materials and operating conditions, *Sustainable Energy Fuels*, 2020, **4**, 2114–2133, DOI: **10.1039/c9se01240k**; (*b*) C. Santoro, A. Lavacchi, P. Mustarelli, V. Di Noto, L. Elbaz, D. R. Dekel and F. Jaouen, What is next in anion-exchange membrane water electrolyzers? Bottlenecks, benefits, and future, *ChemSusChem*, 2022, **15**, e202200027, DOI: **10.1002/cssc.202200027**.
6 IRENA, Geopolitics of the energy transition: Critical materials, Abu Dhabi: 2023. **https://www.irena.org/Publications/2023/Jul/Geopolitics-of-the-Energy-Transition-Critical-Materials** (accessed December 6, 2023).
7 N. Du, C. Roy, R. Peach, M. Turnbull, S. Thiele and C. Bock, Anion-exchange membrane water electrolyzers, *Chem. Rev.*, 2022, **122**, 11830–11895, DOI: **10.1021/acs.chemrev.1c00854**.
8 F. Razmjooei, A. Farooqui, R. Reissner, A. S. Gago, S. A. Ansar and K. A. Friedrich, Elucidating the performance limitations of alkaline electrolyte membrane electrolysis: dominance of anion concentration in membrane electrode assembly, *ChemElectroChem*, 2020, **7**, 3951, DOI: **10.1002/celc.202000605**.
9 R. Ciriminna and M. Pagliaro, Enhanced nickel catalysts for producing electrolytic hydrogen, *RSC Sustain.*, 2023, **1**, 1386–1393, DOI: **10.1039/d3su00177f**.

10 IRENA, Green hydrogen cost reduction, Abu Dhabi: 2020. https://www.irena.org/publications/2020/Dec/Green-hydrogen-cost-reduction (accessed December 6, 2023).
11 (*a*) D. Avnir, Recent progress in the study of molecularly doped metals, *Adv. Mater.*, 2018, **30**, 1706804, DOI: 10.1002/adma.201706804; (*b*) D. Avnir, Molecularly doped metals, *Acc. Chem. Res.*, 2014, **47**, 579–592, DOI: 10.1021/ar4001982.
12 N. Ralbag, M. Mann-Lahav, E. S. Davydova, U. Ash, R. Galed, M. Handl, R. Hiesgen, E. Magliocca, W. Mustain, J. He, P. Cong, A. M. Beale, G. S. Grader, D. Avnir and D. R. Dekel, Composite materials with combined electronic and ionic properties, *Matter*, 2019, **1**, 959–975, DOI: 10.1016/j.matt.2019.04.007.
13 N. K. Mahale and S. T. Ingle, Electrocatalytic hydrogen evolution reaction on nano-nickel decorated graphene electrode, *Energy*, 2017, **119**, 872–878, DOI: 10.1016/j.energy.2016.11.053.
14 T. V. Vineesh, S. Mubarak, M. Gwan Hahm, V. Prabu, S. Alwarappan and T. N. Narayanan, Controllably alloyed, low density, free-standing Ni-Co and Ni-graphene sponges for electrocatalytic water splitting, *Sci. Rep.*, 2016, **6**, 31202, DOI: 10.1038/srep31202.
15 A. Han, S. Jin, H. L. Chen, H. X. Ji, Z. J. Sun and P. W. Du, A robust hydrogen evolution catalyst based on crystalline nickel phosphide nanoflakes on three-dimensional graphene/nickel foam: high performance for electrocatalytic hydrogen production from pH 0-14, *J. Mater. Chem. A*, 2015, **3**, 1941–1946, DOI: 10.1039/c4ta06071g.
16 M. Formenti, M. Pagliaro, C. Della Pina and R. Ciriminna, Graphene oxide in palladium nanoparticle (GrafeoPlad): a new class of catalytic materials for heterogeneous catalysis, *ChemRxiv*, 2023, DOI: 10.26434/chemrxiv-2023-hw1tj.
17 D. R. Dreyer, A. D. Todd and C. W. Bielawski, Harnessing the chemistry of graphene oxide, *Chem. Soc. Rev.*, 2014, **43**, 5288–5301, DOI: 10.1039/c4cs00060a.
18 (*a*) S. Thandiwe, N. Freeman and F. Thabo, The removal of Ni and Cu from a mixed metal system using sodium borohydride as a reducing agent, *S. Afr. J. Chem. Eng.*, 2015, **20**, 16–29; (*b*) Y. Ling Lo and B. J. Hwang, Decomposition of $NaBH_4$ in an electroless nickel bath, *Ind. Eng. Chem. Res.*, 1994, **33**, 56–61, DOI: 10.1021/ie00025a008.
19 M. E. Foster, I. Kendrick, S. Mukerjee and R. Jones, Role of graphene on Ni/NiO for the hydrogen evolution reaction, *J. Phys. Chem. C*, 2022, **126**, 16158–16163, DOI: 10.1021/acs.jpcc.2c04033.
20 Y. Bai, Y. Wu, X. Zhou, Y. Ye, K. Nie, J. Wang, M. Xie, Z. Zhang, Z. Liu, T. Cheng and C. Gao, Promoting nickel oxidation state transitions in single-layer NiFeB hydroxide nanosheets for efficient oxygen evolution, *Nat. Commun.*, 2022, **13**, 6094, DOI: 10.1038/s41467-022-33846-0.
21 R. Ciriminna, M. Formenti, M. Pagliaro and C. Della Pina, Practical aspects concerning catalysis with molecularly doped metals, *ChemCatChem*, 2023, **15**, e202300600, DOI: 10.1002/cctc.202300600.
22 J. Hu, D. Jiang, Z. Weng, Y. Pan, Z. Li, H. Du and Y. Yuan, A universal electrochemical activation enabling lattice oxygen activation in nickel-based catalyst for efficient water oxidation, *Chem. Eng. J.*, 2022, **430**, 132736, DOI: 10.1016/j.cej.2021.132736.
23 Y. Kim and B. E. Logan, Hydrogen production from inexhaustible supplies of fresh and salt water using microbial reverse-electrodialysis electrolysis cells, *Proc. Natl. Acad. U.S.A.*, 2011, **108**, 16176–16181, DOI: 10.1073/pnas.1106335108.
24 A. Mazzone, M. Lopresti, B. D. Belviso and R. Caliandro, New features of the RootProf program for model-free analysis of unidimensional profiles, *J. Appl. Crystallogr.*, 2023, **56**, 1841–1854, DOI: 10.1107/S1600576714005895.
25 A. Altomare, N. Corriero, C. Cuocci, A. Falcicchio, A. Moliterni and R. Rizzi, QUALX2.0: a qualitative phase analysis software using the freely available database POW_COD, *J. Appl. Crystallogr.*, 2015, **48**, 598–603, DOI: 10.1107/S1600576715002319.
26 A. Altomare, C. Cuocci, C. Giacovazzo, A. Moliterni, R. Rizzi, N. Corriero and A. Falcicchio, *EXPO2013*: a kit of tools for phasing crystal structures from powder data, *J. Appl. Crystallogr.*, 2013, **46**, 1231–1235, DOI: 10.1107/S0021889813013113.
27 C. Prescher and V. B. Prakapenka, DIOPTAS: a program for reduction of two-dimensional X-ray diffraction data and data exploration, *High Pres. Res.*, 2015, **35**, 223–230, DOI: 10.1080/08957959.2015.1059835.
28 P. Juhás, T. Davis, C. L. Farrow and S. J. L. Billinge, PDFgetX3: a rapid and highly automatable program for processing powder diffraction data into total scattering pair distribution functions, *J. Appl. Crystallogr.*, 2013, **46**, 560–566, DOI: 10.1107/S0021889813005190.
29 C. L. Farrow, P. Juhás, J. W. Liu, D. Bryndin, E. S. Božin, J. Bloch, T. Proffen and S. J. L. Billinge, PDFfit2 and PDFgui: computer programs for studying nanostructure in crystals, *J. Phys.: Condens. Matter*, 2007, **19**, 335219, DOI: 10.1088/0953-8984/19/33/335219.
30 P. Juhás, C. L. Farrow, X. Yang, K. R. Knox and S. J. L. Billinge, Complex modeling: a strategy and software program for combining multiple information sources to solve ill posed structure and nanostructure inverse problems, *Acta Crystallogr. A*, 2015, **71**, 562–568, DOI: 10.1107/S2053273315014473.